CHAPTER III

SYNTHESIS OF CERIA-ZIRCONIA MIXED OXIDE FROM CERIUM AND ZIRCONIUM GLYCOLATES VIA SOL-GEL PROCESS AND ITS REDUCTION PROPERTY

(Applied Organometallic Chemistry, 2(10) (2006) 615-625)

3.1 Abstract

Ceria-zirconia mixed oxide was successfully synthesized via sol-gel process at ambient temperature, followed by calcination at 500°, 700° and 900°C. The synthesis parameters, such as, alkoxide concentration, aging time, and heating temperature, were studied to obtain the most uniform and remarkably high-surface-area cubic-phase mixed oxides. Thermal stability of both oxides was enhanced by mutual substitution. Surface areas of the $Ce_xZr_{1-x}O_2$ powders were improved by increasing ceria content, and their thermal stability was increased by the incorporation of ZrO_2. The most stable cubic phase solid solutions were obtained in the Ce range above 50 mol%. The highest surface area was obtained from the mixed catalyst containing a ceria content of 90 mol% ($200m^2/g$). TPR results show that increasing the amount of Zr in the mixed oxides results in a decrease in the reduction temperature, and that the splitting of the support reduction process into two peaks depends on CeO_2 content. The CO oxidation activities of samples were related to its composition. The activities of catalysts for this reaction decrease with a decrease of Zr amount in cubic phase catalysts. $Ce_6Zr_4O_2$ exhibited the highest activity for CO oxidation.

Keywords: Ceria, Zirconia, Sol-gel process and TPR

3.2 Introduction

Ceria-based materials are widely used in automotive pollution control[1]. Among several tasks carried out by ceria, the most important one is related to its property of being an oxygen buffer. However, one well-known drawback is its low stability in high temperature ranges. Recent studies report the improvement of textural properties by introducing doping elements in the CeO_2 fluorite-type lattice, and the most efficient dopant studied was zirconium, as excellently discussed by Trovarelli *et al.*[2-5] and Fornasiero *et al.*[6-9].

One of the keys to this success is the selection of an appropriate precursor[47, 48], the preparation methods and the composition (i.e. Ce/Zr ratio), which in turn determine homogeneity at a molecular level, surface area and textural/morphological properties. There are many different synthetic methods that have been applied to prepare CeO_2-ZrO_2 and related mixed oxides. These include solid state synthesis[10, 11], co-precipitation[12, 13], high energy ball-milling[14, 15] and sol-gel[16, 17]. The sol-gel process is a versatile technique, allowing control of the texture, composition, homogeneity and structural properties of solids[18]. Generally, Ce-rich compositions are preferred for catalysis purposes and the best results are obtained using $Ce_xZr_{1-x}O_2$ with x ranging from 0.6 to 0.8[19]. The surface areas of ceria-zirconia obtained by either conventional co-precipitation or sol-gel were typically in the range of 60-90 m^2/g after calcinations under air at 700-800 K[5, 7]. Surface areas above 100 m^2/g were reported for materials obtained from CeO_2-ZrO_2 gel prepared at 100°C by Mayoo *et al.*[20]. The objective of this present study was thus to obtain higher surface area and characterize the properties, including the reduction property, of CeO_2-ZrO_2 mixed oxides prepared by sol-gel at ambient temperature. The influences of the composition, aging time and heat treatment on the texture, structure, reduction property and catalytic activity for CO oxidation of the samples were discussed.

3.3 Experimental

3.3.1 Materials

Cerium (IV) hydroxide ($Ce(OH)_4$, 87.4% CeO_2) and zirconium hydroxide ($Zr(OH)_4$, 97% purity) and HCl were purchased from Aldrich Chemical Co. Inc. (USA). Triethylenetetramine (TETA, $NH_2(CH_2CH_2NH)_3H$) was supplied from Carlo Erba Reagent; ethylene glycol (EG, $HOCH_2CH_2OH$) from J.T. Beaker Inc; NaOH from EKA Chemicals; and acetonitrile (CH_3CN) from Lab Scan Co., Ltd. All chemicals were used as received.

3.3.2 Instruments

Elementary analysis was carried out on an X-ray Fluorescence (PW 2400) instument. The structure of the samples was obtained from the wide-angle X-ray diffractometer (WXRD) on D/MAX 2000 Rigaku, using CuK$\propto$ radiation (λ = 1.5406 Å). The intensity data were collected at 25°C over 2θ range of 5-90°. Peak positions were compared with standard JCPDS files to identify crystalline phases. The average grain size (D) was estimated according to the Scherrer equation:

$$D = 0.94\lambda / \beta \cos\theta$$

where, θ is the diffraction angle of the (111) peak of the cubic phase or the (101) peak of the tetragonal phase and β is the full width at half-maximum (fwhm) of the (111) or the (101) peak (in radian)[37]. FT-Raman spectra were obtained on the JOBIN HR 800 FT-Raman Spectrometer using a frequency range of 100-900 cm^{-1}. Scanning electron micrographs (SEM) were obtained on a JOEL 5200-2AE (MP15152001). Surface areas of all powder samples were determined by N_2 adsorption at 77K (five point Brunauer-Emmett-Teller BET method) using a Quantachrome Corporation Autosorb. Prior to analysis, the samples were outgassed at 250°C for 4h. Temperature programmed

reduction (TPR) of catalysts was carried out using 5% hydrogen in nitrogen used as the carrier gas with a flow rate of 50 ml/min. A Micromeritics TPD/TPR 2900 was employed as an analyzer for the temperatures of the thermal conductivity detector, using a furnace temperature up to 900°C at a linear ramp rate of 10°C/min. The sample was pretreated by flowing He over the sample at 120°C for 4h before analysis. An effluent gas steam from the reactor was first dehumidified by cold water-trap before auto-sampling in a gas chromatograph (Agilent Technologies 6890N model). The carbosphere, 80/100 mesh, and 10ft x 1/8-inch stainless packed column were used for separating all components. The results were recorded by Agilent chemstation software. The observed peaks were identified by comparison with the retention time of the standard gas. For quantitative analysis, the peak area was used to determine the concentration of each component based on the calibration curves obtained from known composition gases.

3.3.3 Methodology

Mixed oxide catalysts were prepared via the sol-gel process. Cerium glycolate and sodium tris(glycozirconate) synthesized via the OOPS (Oxide One Pot Synthesis) process were used as precursors[21]. The starting glycolate materials were mixed with 1M hydrochloric solution at 1:1 mole ratio. The ratio between each metal alkoxide was varied, depending on desired compositions: $Ce_xZr_{1-x}O_2$, where x = 0-1. The gel was kept at room temperature for 24 and 168 h, followed by washing with deionized water 3 times to remove the Na content generated from sodium tris(glycozirconate). The samples were then put in an oven at 110°C for at least 12 h to let them dry before calcination at 500°, 700° and 900°C for 2 h in air. The products were characterized for their structures and morphologies using XRD, FT-Raman, SEM, BET and TPR.

The catalytic activity of the synthesized samples was measured using a differential packed bed quartz U-tube reactor (ID 4mm). A mixed oxide sample of 0.1 g was packed between two layers of glass wool. The reactor was placed in a furnace where

the temperature of the catalyst bed was monitored and controlled by PID temperature controller equipped with a type K thermocouple. Exit gases were analyzed chromatographically. Gas mixture (50 ml/min) consisted of 1% CO, 1% O_2 balanced in He and were passed through the catalyst bed at ambient temperature. After stabilization, the temperature of the bed was raised, and the light-off temperature was recorded at the temperature at which the conversion of CO reached 50%.

3.4 Results and Discussion

3.4.1 X-ray Fluorescence

The bulk and micro domain metal compositions in the mixed oxides were determined by XRF measurement. Table 3.1 shows that the experimental Ce content from XRF was in good agreement with the target composition, indicating the good stoichiometric homogeneity of Ce and Zr cations in the calcined products.

3.4.2 X-ray Diffraction

XRD patterns for $Ce_xZr_{1-x}O_2$ mixed oxides calcined at 700° and 900°C in the whole compositional range are compared in Figures 3.1 and 3.2, respectively. At the higher calcination temperature, the narrower diffraction lines indicate better crystallinity and more intensity for the pure oxides. It should be noted that all synthesized oxides calcined at 500° (not shown) or 700°C have similar XRD patterns, except the intensity. Unlike the effect of calcination temperature, the aging time has an insignificant effect on the structure. The XRD patterns are almost the same. Pure oxide CeO_2 is composed of cubic phase at 2θ of 29° (111), 33° (200), 48° (220), 56° (311), 60° (222), and 70° (400) for all calcination temperatures studied. Pure ZrO_2 samples calcined at either 500° or 700°C are composed of tetragonal phase at 2θ = 30°, 35°, 50° and 59°. Additional monoclinic phase appears with the peaks at 2θ = 28.5° and 31.4° after heating at 900°C.

In other words, the monoclinic phase is preferable at higher temperature, which is in good agreement with the results reported elsewhere[22, 23].

In the patterns of the oxides with intermediate composition, the reflections are broader, showing that the crystallite size is smaller. The reflections in these patterns systematically shift, due to shrinkage of the lattice, to lower *d*-spacing when cerium is replaced by zirconium. This shrinkage phenomenon coincides with the fact that the cation radius of Zr^{4+}(0.84 Å) is smaller than that of Ce^{4+}(0.97 Å)[24]. By progressively doping ZrO_2 with CeO_2, the tetragonal structure modification is maintained for the content of 20% ceria with no splitting or asymmetry of the peaks being recorded for all three temperature treatments. For $Ce_xZr_{1-x}O_2$, where $0.3 \leq x \leq 0.5$, the patterns are still the same for samples calcined at 500° and 700°C. But for 900°C, the segregate peaks of cubic phases appear, resulting from heterogeneity in phase composition.

Going further toward CeO_2 in the composition scale, the symmetry corresponds increasingly to the cubic one. The results show that $Ce_xZr_{1-x}O_2$, where $x > 0.5$, presents only the cubic phase in the samples calcined at all heat treatments, in agreement with the result of Alfanti *et al.*[25] and Yamashima *et al.*[26].

Since mixed oxides obtained give broadening peaks from powder X-ray diffraction, meaning that the symmetry of solid solution phases or the co-presence of some amounts of tetragonal phases in Ce-rich samples cannot be determined accurately by using XRD, raman spectroscopy was thus employed to confirm their composition. Moreover, the XRD patterns in Zr-rich samples calcined at 500° and 700°C also show broadening diffractions above interesting regions, probably informing some multiplicity[24]. In addition, according to Duvez and Odell, the mutual solubility of ZrO_2 and CeO_2 is very limited below 1,000°C, based on thermodynamics. A mixture of zirconia-rich tetragonal phase and ceria-rich cubic phase is expected in the compositional range above 20% ceria[27]. The particle sizes (*D*) from the XRD for $Ce_xZr_{1-x}O_2$ (x = 0-1) powders are listed in Table 3.2. The result shows that the *D* value of the

mixed oxides decreased with the doping of ZrO_2. The particle sizes of mixed oxides are increased after calcination at higher temperature due to the sintering process.

3.4.3 FT-Raman Spectroscopy

The Raman spectra of the mixed oxide catalysts, using the aging times 24 and 168 h, appear very similar. The patterns of samples calcined at 500° (not given) and 700°C are nearly identical, whereas the spectra of $Ce_xZr_{1-x}O_2$ mixed oxides calcined at 700° and 900°C are shown in Figures 3.3 and 3.4, respectively.

The spectrum for pure ceria displays only one peak at 465 cm^{-1}, as expected on the basis of the factor group analysis and in agreement with the results indicated in Reference 28-30. This peak corresponds to the fundamental with F2g symmetry, which can be regarded as a symmetric O-Ce-O stretching. For pure zirconia, peaks at 147, 268, 313, 460, 600 and 645 cm^{-1} appeared. Those are the six raman bands predicted for theoretical tetragonal zirconia, and these results agree with other references[31, 32]. The bands in Figure 4 at 180, 334, 475 cm^{-1} are characteristic of the monoclinic phase[33]. The bands at 268 and 180 cm^{-1} are found only in t-ZrO_2 and m-ZrO_2, respectively[34], confirming the mixed phases between tetragonal and monoclinic phases of ZrO_2 after heating at 900°C.

The Raman spectra for the samples containing up to 40% zirconia do not vary significantly with respect to that of pure ceria, and show only one peak at 465 cm^{-1}, characteristic of the cubic fluorite-like structure, in agreement with the XRD analysis. Conversely, when the Zr content rises above 40%, the main peak in the spectra decreases in intensity and disappears when Zr amount increases higher than 70% for the samples calcined at 500° and 700°C, whereas the six predicated characteristic bands of the tetragonal symmetry occur at about 145, 265, 315, 465, 600 and 635 cm^{-1} for samples calcined at 900°C. These new spectral features are presumably due to a partial tetragonalization of the sample[35]. The spectra for the composition of mixed oxides having zirconia content between 50-70 mol% suggest the co-presence of a tetragonal

and a cubic solid solution phase; as the band at 465 cm^{-1} is observed together with the tetragonal phase, though the cubic phase is still largely predominant. In addition, the two weak bands at around 130 and 620 cm^{-1}, attributed to the presence of defective structures in CeO_2-ZrO_2 materials, suggest the absence of defective structure in its crystal lattice after the sintering process[36].

3.4.4 SEM and BET Investigation

SEM allows picturing the morphology of the materials directly. All samples prepared by sol-gel have a spongy appearance, as shown in Figure 3.5. The calcination process occurs easier for $Ce_{0.9}Zr_{0.1}O_2$ than $Ce_{0.6}Zr_{0.4}O_2$. However, the pure oxides are sintered the easiest. This aggregation caused the reduction in surface area of the samples. BET surface areas of catalysts in Figure 3.6 show that the BET surface area of the mixed oxides calcined at 500°, 700° and 900°C are higher than those of pure oxides. The surface areas of $Ce_xZr_{1-x}O_2$ mixed oxides increase when increasing the ceria content up to 90 mol%. The highest surface area obtained is from $Ce_{0.9}Zr_{0.1}O_2$ ($200.14 m^2g^{-1}$) after calcination at 500°C, which is higher than other works using sol-gel[20, 25, 37]. This result is totally the opposite of the study reported by Cuif *et al.*[38]. It can be explained by the fact that surface areas, particle morphology, having different degrees of homogeneity, and even the phase nature of mixed oxide are strongly affected by the synthesis conditions. In the co-precipitation derived ceria-zirconia solid solutions studied by Trovarelli and coworkers[39], the specific surface area increased upon substituting zirconia. Figure 3.7 shows that the thermal stability of mixed oxides is increased when increasing the amount of zirconia up to 40%. This can be explained by the following: the addition or incorporation of zirconia to ceria as mixed oxides can enhance the thermal stability of CeO_2, resulting in better resistance of the sintering and deactivation processes. It is clear that CeO_2 undergoes a rapid crystallite growth process since BET surface areas of both catalysts using the aging times of 24 and 168 h decrease significantly more than those of mixed oxide samples. Therefore, the crystallite growth

process is retarded by the incorporation of Zr ion into the CeO_2 matrix. For $Ce_xZr_{1-x}O_2$, x $\leq$ 0.5, the % loss of surface area is nearly the same. The reason is related to the homogeneity of the samples. Formation of homogeneous solid solution over the whole range of composition by using a single method is unreliable[40, 41]. In this work the homogeneous solid solutions were obtained for Zr molar contents up to 40%. The surface areas of the catalysts aged for 24h are higher than those of 168h, since the hydrolysis and condensation in the sol-gel process is one of the keys to obtaining high surface area.

3.4.5 Temperature Programmed Reduction (TPR)

The reactivity of lattice oxygen in ceria zirconia mixed oxide catalysts towards H_2 was investigated by TPR technique (Figures 3.8). The TPR profile of CeO_2 shows the two-peak pattern due to surface (low temperature peak), and bulk reduction (high temperature peak)[4, 42]. In contrast with CeO_2, only a very small amount of H_2 was consumed for ZrO_2 because its structure was tetragonal, which is almost irreducible. In the mixed oxides, broad peaks are shown, in agreement with the promotion of the reduction in the bulk of mixed oxide upon doping zirconia. Many researchers suggest that surface and bulk reduction cannot be distinguished by the conventional TPR technique since both processes occur almost simultaneously during TPR measurement[43, 44]. Obviously, such a peak could not be ascribed only to the reduction of the surface oxygen because of the dominant H_2 consumption of the low temperature peaks. The reduction of the bulk lattice oxygen in the solid solution becomes easier because of the distortion of the structure, which is caused by the partial substitution of Ce^{4+} with Zr^{4+} in the sol-gel technique. As a result, reduction of the bulk lattice oxygen must occur simultaneously with the reduction of surface oxygen. This occurs through structural modifications of the fluorite-type lattice of ceria as a consequence of the substitution of Ce^{4+} (ionic radius 0.97 A) with Zr^{4+} (ionic radius 0.84 A). The effect of this substitution is to decrease cell volume, lowering the activation energy for oxygen-ion diffusion

within the lattice, and consequently favoring reduction. The introduction of Zr also enhances the formation of structural defects that are expected to play an important role in determining reduction/oxidation behavior. This result is in agreement with many previous works[45, 46]. It clearly appears from the TPR results that the lowest reduction temperatures are observed and that in the cubic structure the reduction process is kinetically favored compared to the tetragonal one[47].

3.4.6 CO oxidation

The results showed that the activity of the mixed oxides calcined at 900° and 700°C are incomparable to those of mixed oxides calcined at 500°C, whereas light-off temperature could not be achieved at temperature below 400°C. This is due to the fact that surface areas of mixed oxides calcined at 900° and 700°C are significantly lower compared to that of mixed oxides calcined at 500°C. In the case of aging time, it was also found that it has no effect on the CO oxidation. Figure 3.9 shows that the catalytic activity of the prepared sample was found to decrease with a decrease of Zr content in the cubic phase Ce-rich region. In fact, all of the Ce-rich mixed oxides synthesized in this study have only cubic phase. However, in the Zr-rich region the catalytic activity is lower compared to the Ce-rich region because the cubic phase provides easier reduction than the tetragonal one. The presence of tetragonal phase is not preferred in catalytic applications[20]. It can be postulated that the catalytic activity has no direct correlation with surface area since $Ce_6Zr_4O_2$ exhibits the highest activity for CO oxidation while having lower surface area than those mixed oxides having Ce molar content between 60 - 90%. This is in a good agreement with the study cited in Reference 23 showing that the activity of the Ce-Zr mixed oxides is nearly related to their reducibility.

3.5 Conclusions

On the basis of the XRD and FT Raman results, the most homogeneous samples are in the ceria-rich compositions. The monoclinic phase is present only in the case of pure zirconia after calcination at 900°C. For a zirconia content in the range of 50-90 mol%, the dissolution of ZrO_2 into the CeO_2 lattice was observed with the formation of a fluorite structured with a partial tetragonalization for higher zirconium loading. Surface area increases with the increased ceria content up to 90 mol%, and an increase of zirconia increases the surface area stability up to 40 mol%. The sol-gel process can prepare high surface area mixed oxide. Moreover this method is easy to apply and no heat is required. Reciprocal substitution of the two oxides enhances the thermal stability of the single oxide, especially in the Ce-rich region. TPR results show that an increase in the amount of zirconium molar content results in a decrease in the reduction temperature for mixed oxides, which have zirconia molar content between 10-40 mol%, and the splitting of the support reduction process into two peaks clearly depends on CeO_2 content. The CO oxidation activities of mixed oxides were related to its composition. The cubic phase mixed oxides could be reduced easier than the tetragonal phase. It can be speculated that a solid solution of ceria-zirconia in a cubic phase is a good catalyst for CO oxidation. There is no segregation of CeO_2 from the mixed oxides after the reaction.

3.6 Acknowledgments

The authors gratefully acknowledge the financial support of the Postgraduate Education and Research Program in Petroleum and Petrochemical Technology, the PPT Consortium (ADB) Fund and the Ratchadapisake Sompote Fund, Chulalongkorn University.

3.7 References

1. A. Trovarelli, C. De Leitenburg, M. Boaro, G. Dolcetti, Catal. Today 50 (1999) 353.
2. Maschio, S.; Trovarelli, A. Br. Ceram. Transac. 1995, 94, 191.
3. Trovarelli, A.; de Leitenburg, C.; Dolcetti, G. Chemtech 1997, 32.
4. Trovarelli, A.; Zamar, F.; Llorca, J.; de Leitenburg, C; Dolcetti, G.; Kiss, J. T. J. Catal. 1997, 169, 490.
5. Leitenburg, C.; Trovarelli, A.; Llorca, J.; Cavani, F.; Bini, G. Appl. Catal. A: General 1996, 139, 161.
6. Fornasiero, P.; Di Monte, R.; Ranga Rao, G.; Kaspar, J.; Meriani, S.; Trovarelli, A.; Graziani, M. J. Catal. 1995, 151, 168.
7. Fornasiero, P.; Balducci, G.; Di Monte, R.; Kaspar J.; Gubitosa, G.; Ferrero, A.; Graziani, M. J. Catal. 196, 164, 173.
8. Fornasiero, P.; Balducci, G.; Meriani, S.; Di Monte, R.; Graziani, M. Catal. Today 196, 29, 47.
9. Fornasiero, P.; Kaspar, J.; Sergo, v.; Graziani, M. J. Catal. 1999, 182, 56
10. R. Ranga, J. Kaspar, R. Di Monte, S. Meriani, M. Graziani, Catal. Lett. 24 (1994) 107.
11. P. Fornasiero, R. Di Monte, R. Ranga, J. Kaspar, S. Meriani, A. Trovarelli, M. Graziani, J. Catal. 151 (1995) 168.
12. M.Y. Sinev, G.W. Graham, L.P. Haack, M. Shelef, J. Mater. Res. 11 (1996) 1960.
13. T. Murota, T. Hasegawa, S. Aozasa, H. Matsui, M. Motoyama, J. Alloys Comp. 193 (1993) 298.
14. Y.L. Chen, M. Qi, D.Z. Yang, K.H. Wu, Mater. Sci. Eng. A 183 (1994) L9.
15. D. Michel, L. Mazerolles, P. Berthet, E. Gaffet, J. Am. Ceram. Soc. 76 (1993) 2884.
16. V.S. Nagarajan, K.J. Rao, Phil. Mag. A 65 (1992) 771.
17. Y. Sun, P.A. Sermon, J. Mater. Chem. 6 (1996) 1025.
18. M.A. Cauqui, J.M. Rodriguez-Izquierdo, J. Non-Cryst. Solids 147/148 (1992) 724.
19. A. Trovarelli, Catal. Rev-Sci. Eng. 38 (1996) 439.

20. M. Thammachart, V. Meeyoo,Catalysis, T. Risksomboon, S. Osuwan, Catal. Today 68 (2001) 53.
21. Ksapabutr B, Gulari E, Wongkasemjit S, Mater. Chem. and Phy. 83(2004) 34.
22. J. Kaspar, S. Meriani, A. Trovarelli, M. Graziani, J. Catal. 151 (1995) 168.
23. D. Terribile, A. Trovarelli, J. Liorca, C. de Leitenburg, G. Dolcetti, Catal. Today 43 (1998) 79.
24. V. Sanchez Escribano. Solid State Sci. 5 (2003) 1369.
25. M. Alifanti, B. Baps, N. Blangenois, J. Naud, P. Grange, B. Delmon, Chem. Mater. 2003, 15, 395-403
26. Yashima, M.; Ohtake, K.; Kakihana, M.; Yoshimura, M. J. Am. Ceram. Soc. 1994, 77, 2773.
27. P. Duwez, F. Odell, J. Am. Ceram. Soc. 33 (9) (1950) 280.
28. W.H. Weber, K.C. Hass, J.R. McBride, Phys. Rev. B 48 (1993) 178.
29. S. Kanakaraju, S. Mohan, A.K. Sood, Thin Solid Films 305 (1997) 191.
30. S. Wang, W. Wang, J. Zuo, Y. Qian, Mater. Chem. Phys. 68 (2001) 246.
31. T. Hirata, E. Asari, M. Kitajima, J. Solid State Chem. 110 (1994) 201.
32. E. Finocchio, M. Daturi, C. Binet, J.C. Lavalley, G. Blanchard, Catal. Today 52 (1999) 53
33. V. Keramidas, H. Jung, I. Yang, J. Am. Ceram. Soc. 57, 22 (1974).
34. Meijun Li, Zhaochi Feng, Guang Xiong, Pinliang Ying, Qin Xin, and Can Li J. Phys. Chem. B, 105 (34), 8107 -8111, 2001.
35. Kim, D.-J., Jung, H.-J., and Yang, I.-N., J. Am. Ceram. Soc. 76, 2106 (1993); Hirata, T., Asari, E, and Kitajima, M., J. Solid State Chem. 110, 201 (1994).
36. Yashima, M.; Arashi, H.; Kakihana, M.; Yoshimura, M. J. Am. Ceram. Soc. 1994, 77, 1067
37. Rui Si, Ya-Wen Zhang, Shi-Jie Li, Bing-Xiong Lin, and Chun-Hua Yan. J. Phys. Chem. B, 108 (2004) 12481.
38. J.P. Cuif, G. Blanchard, O. Touret, A. Seigneurin, SAE 970463 (1997).

39. A. Trovarelli, C. De Leitenburg, G. Dolcetti, J. Chem. Soc., Chem. Commun. (1995) 965.
40. J. Kaspar, P. Fornasiero, M. Graziani Catal. Today 50 (1999) 285.
41. S. Rossignol, Y. Madier, D. Duprez Catal. Today 50 (1999) 261.
42. Yao, H.C.; Yu Yao, Y.F. J. Catal. 86 (1984) 254.
43. P. Vidmar, J. Kaspar, P. Fornasiero, M. Graziani J. Phys. Chem. B 102 (1998) 557.
44. J. Kaspar, P. Fornasiero, M. Graziani, F. Vidal, J. Catal. 164 (1996) 173.
45. J. Kaspar, P. Fornasiero, M. Graziani, A. Trovarelli, J. Catal. 151 (1995) 168.
46. J. Kaspar, H. Vidal, M. Daturi, E. Finocchio, C. Binet J. Phys. Chem. B 104 (2000) 9186.
47. Khushalani, D., Ozin, G.A., Kuperman, A. J. Mater. Chem. 1999, 9, 1483.
48. Khushalani, D., Ozin, G.A., Kuperman, A. J. Mater. Chem. 1999, 9, 1491.

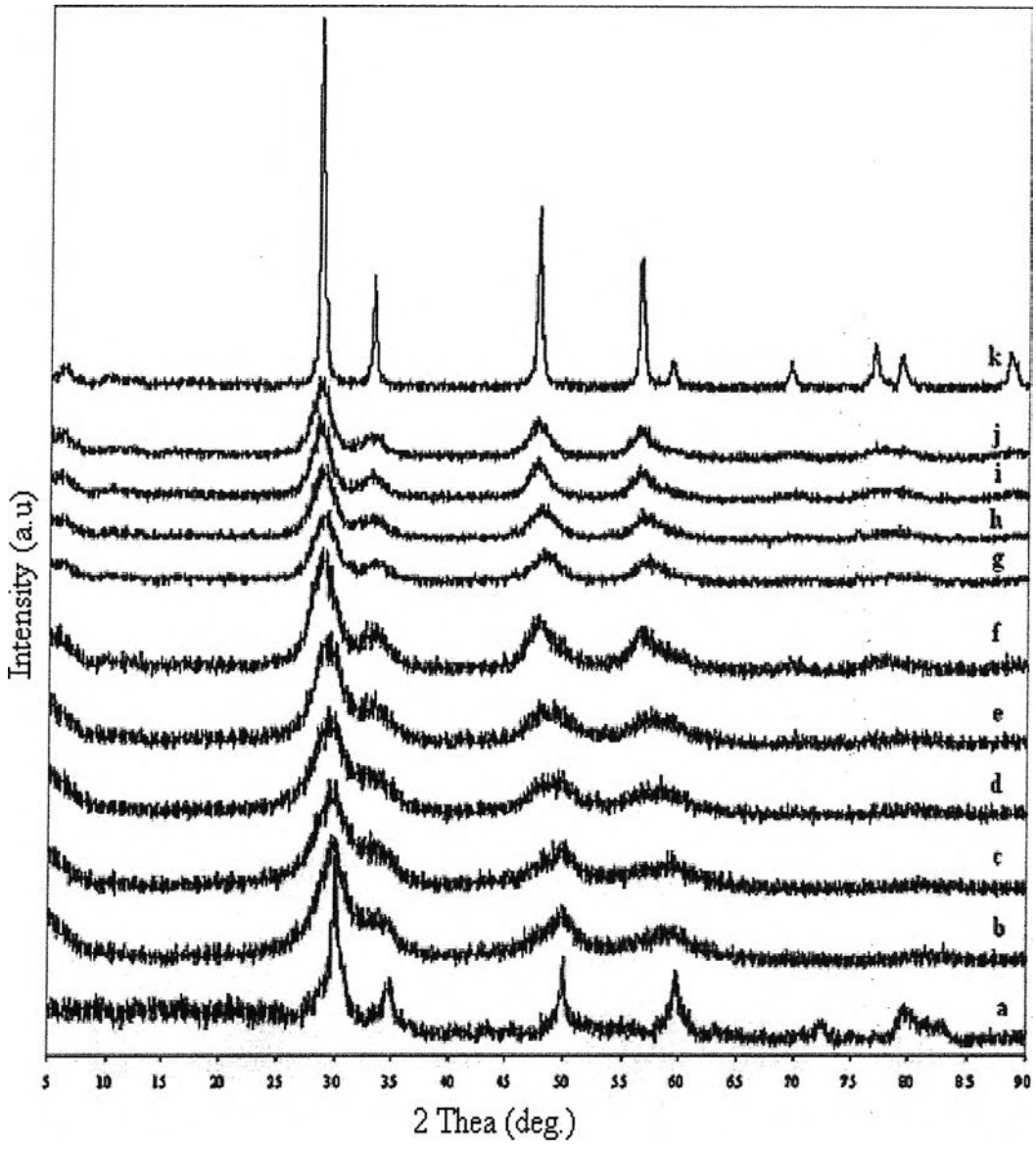

Figure 3.1 XRD patterns for ceria-zirconia mixed oxides with the aging time = 24 h and calcined at 700°C: (a) ZrO_2; (b) $Ce_{0.1}Zr_{0.9}$; (c) $Ce_{0.2}Zr_{0.8}$; (d) $Ce_{0.3}Zr_{0.7}$; (e) $Ce_{0.4}Zr_{0.6}$; (f) $Ce_{0.5}Zr_{0.5}$; (g) $Ce_{0.6}Zr_{0.4}$; (h) $Ce_{0.7}Zr_{0.3}$; (i) $Ce_{0.8}Zr_{0.2}$; (j) $Ce_{0.9}Zr_{0.1}$; (k) CeO_2.

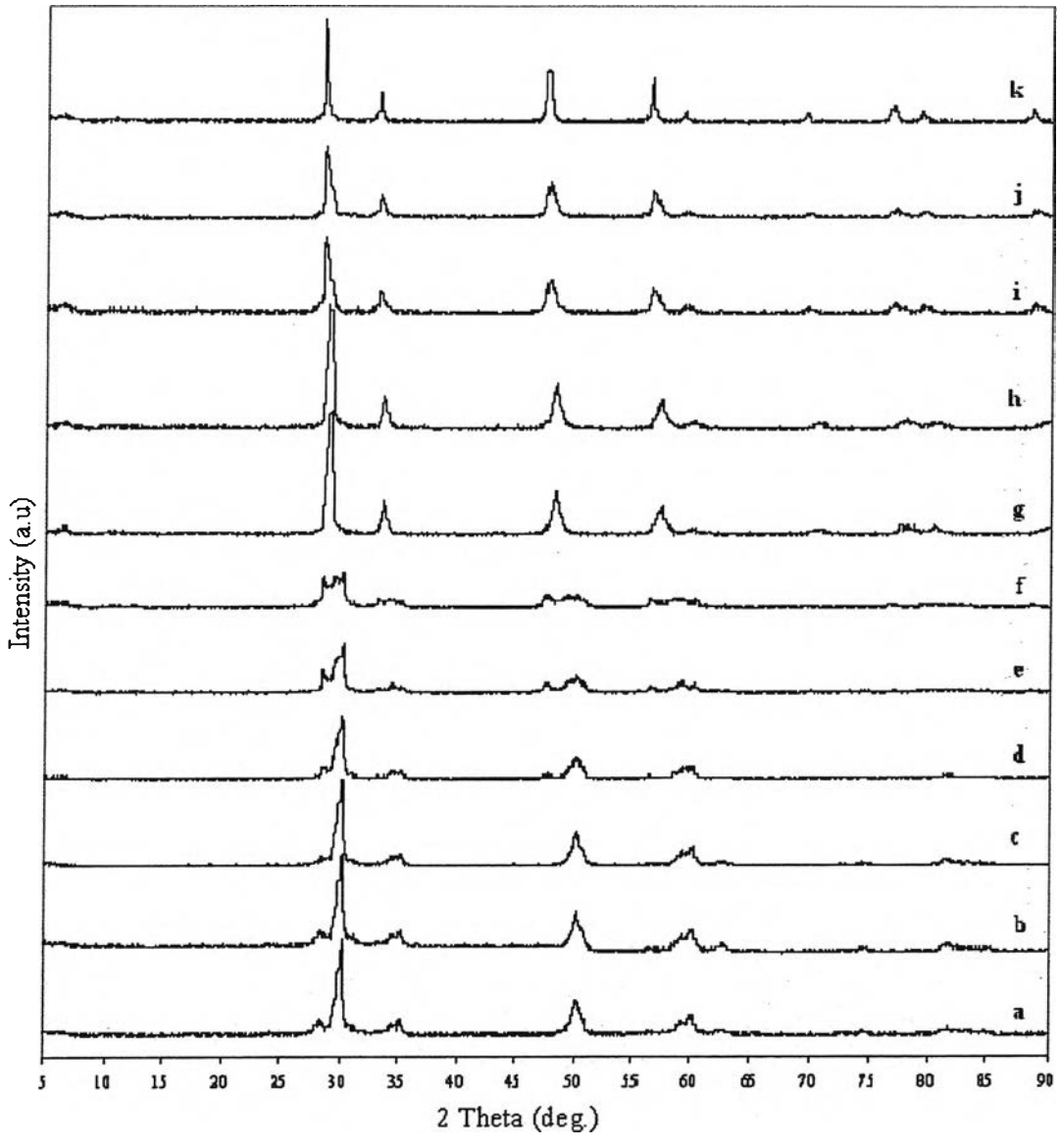

Figure 3.2 XRD patterns for ceria-zirconia mixed oxides with the aging time = 24 h and calcined at 900°C: (a) ZrO_2; (b) $Ce_{0.1}Zr_{0.9}$; (c) $Ce_{0.2}Zr_{0.8}$; (d) $Ce_{0.3}Zr_{0.7}$; (e) $Ce_{0.4}Zr_{0.6}$; (f) $Ce_{0.5}Zr_{0.5}$; (g) $Ce_{0.6}Zr_{0.4}$; (h) $Ce_{0.7}Zr_{0.3}$; (i) $Ce_{0.8}Zr_{0.2}$; (j) $Ce_{0.9}Zr_{0.1}$; (k) CeO_2.

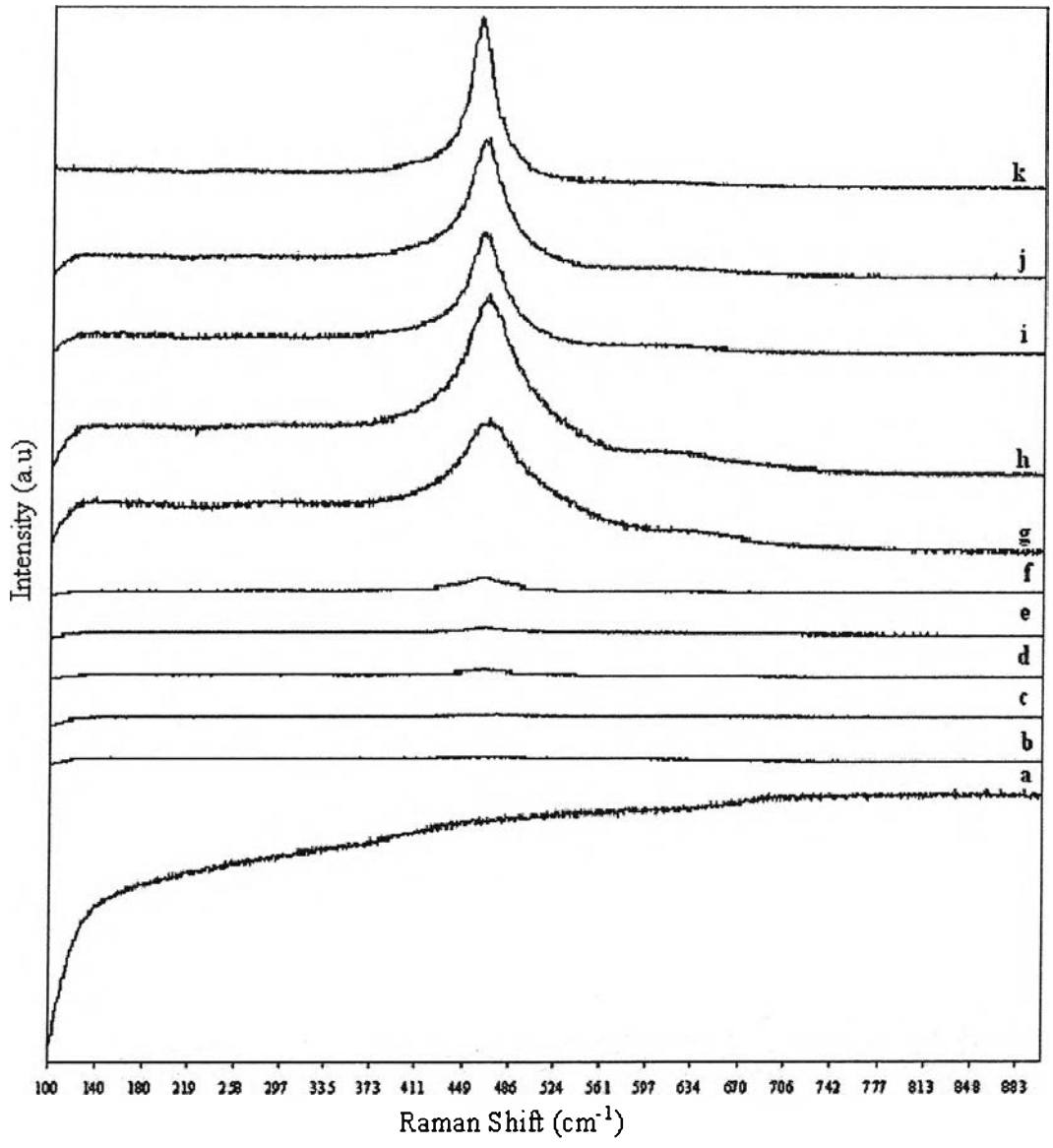

Figure 3.3 FT-Raman spectra for ceria-zirconia mixed oxides with the aging time = 24 h and calcined at 700°C: (a) ZrO_2; (b) $Ce_{0.1}Zr_{0.9}$; (c) $Ce_{0.2}Zr_{0.8}$; (d) $Ce_{0.3}Zr_{0.7}$; (e) $Ce_{0.4}Zr_{0.6}$; (f) $Ce_{0.5}Zr_{0.5}$; (g) $Ce_{0.6}Zr_{0.4}$; (h) $Ce_{0.7}Zr_{0.3}$; (i) $Ce_{0.8}Zr_{0.2}$; (j) $Ce_{0.9}Zr_{0.1}$; (k) CeO_2.

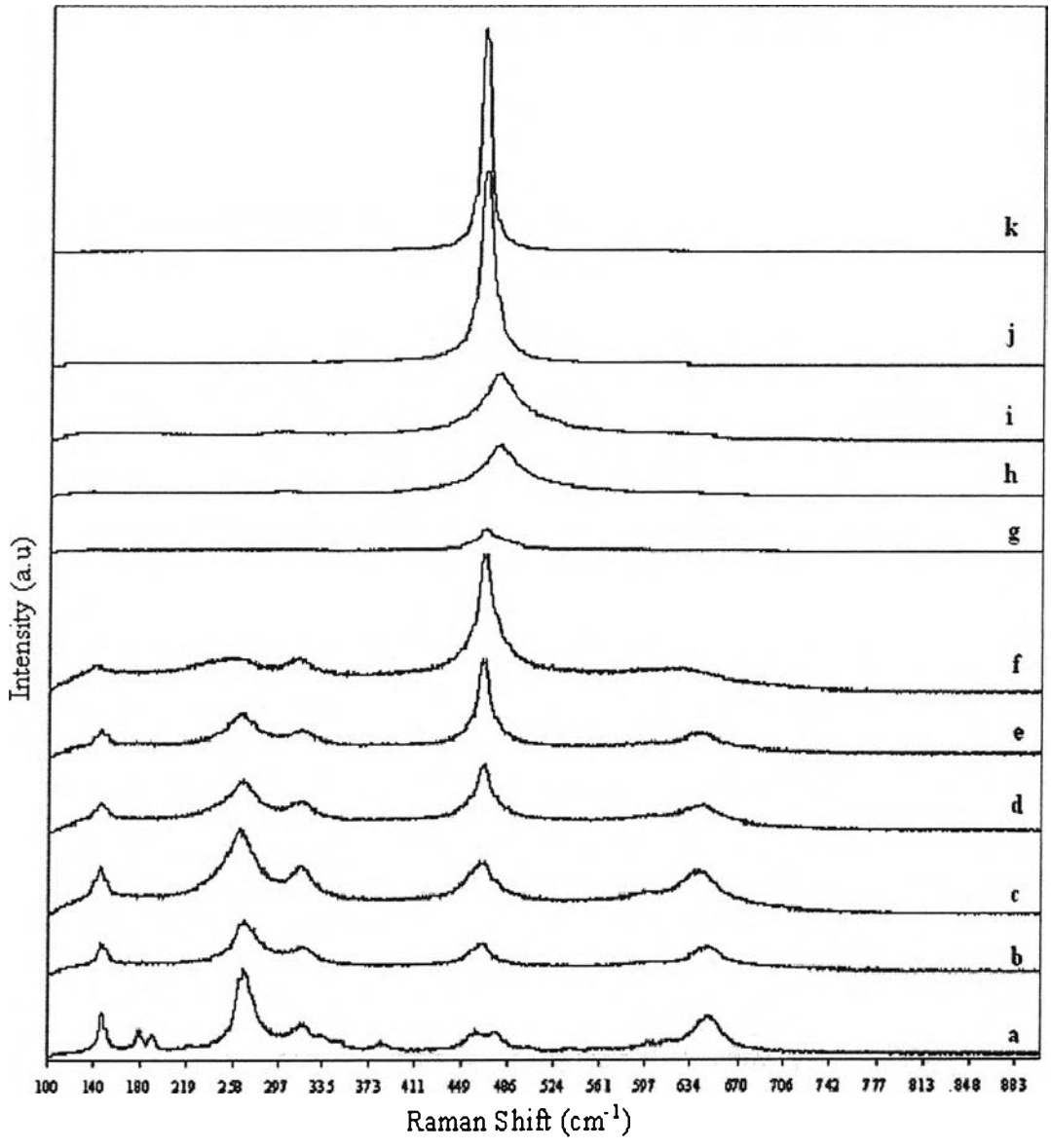

Figure 3.4 FT-Raman spectra for ceria-zirconia mixed oxides with the aging time = 24 h and calcined at 900°C: (a) ZrO_2; (b) $Ce_{0.1}Zr_{0.9}$; (c) $Ce_{0.2}Zr_{0.8}$; (d) $Ce_{0.3}Zr_{0.7}$; (e) $Ce_{0.4}Zr_{0.6}$; (f) $Ce_{0.5}Zr_{0.5}$; (g) $Ce_{0.6}Zr_{0.4}$; (h) $Ce_{0.7}Zr_{0.3}$; (i) $Ce_{0.8}Zr_{0.2}$; (j) $Ce_{0.9}Zr_{0.1}$; (k) CeO_2.

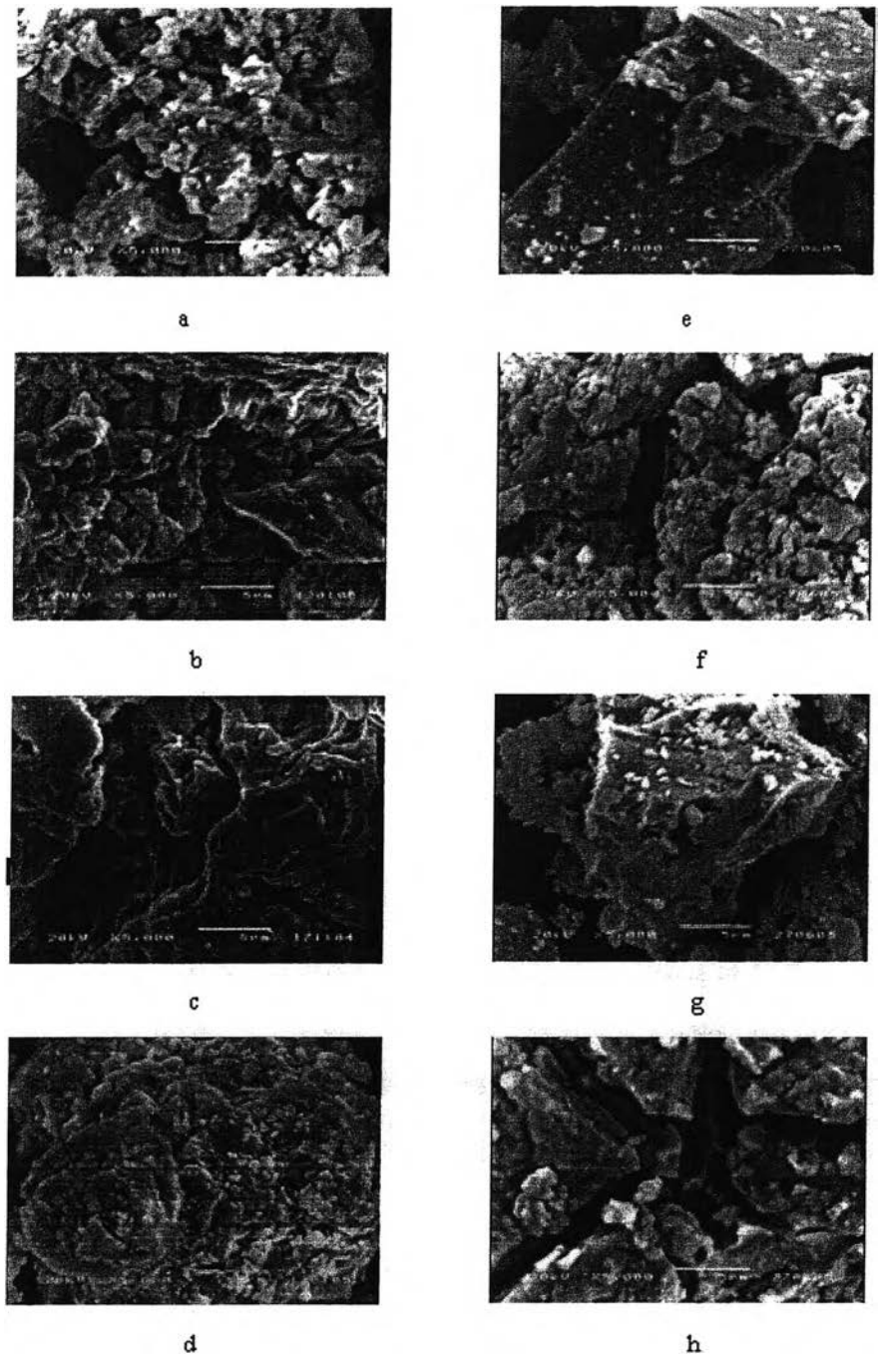

Figure 3.5 SEM picture of ceria-zirconia mixed oxides with the aging time = 24 h and calcined at 500°C: (a) CeO_2; (b) $Ce_{0.6}Zr_{0.4}$; (c) $Ce_{0.9}Zr_{0.1}$; (d) ZrO_2; calcined at 900°C: (e) CeO_2; (f) $Ce_{0.6}Zr_{0.4}$; (g) $Ce_{0.9}Zr_{0.1}$; (h) ZrO_2.

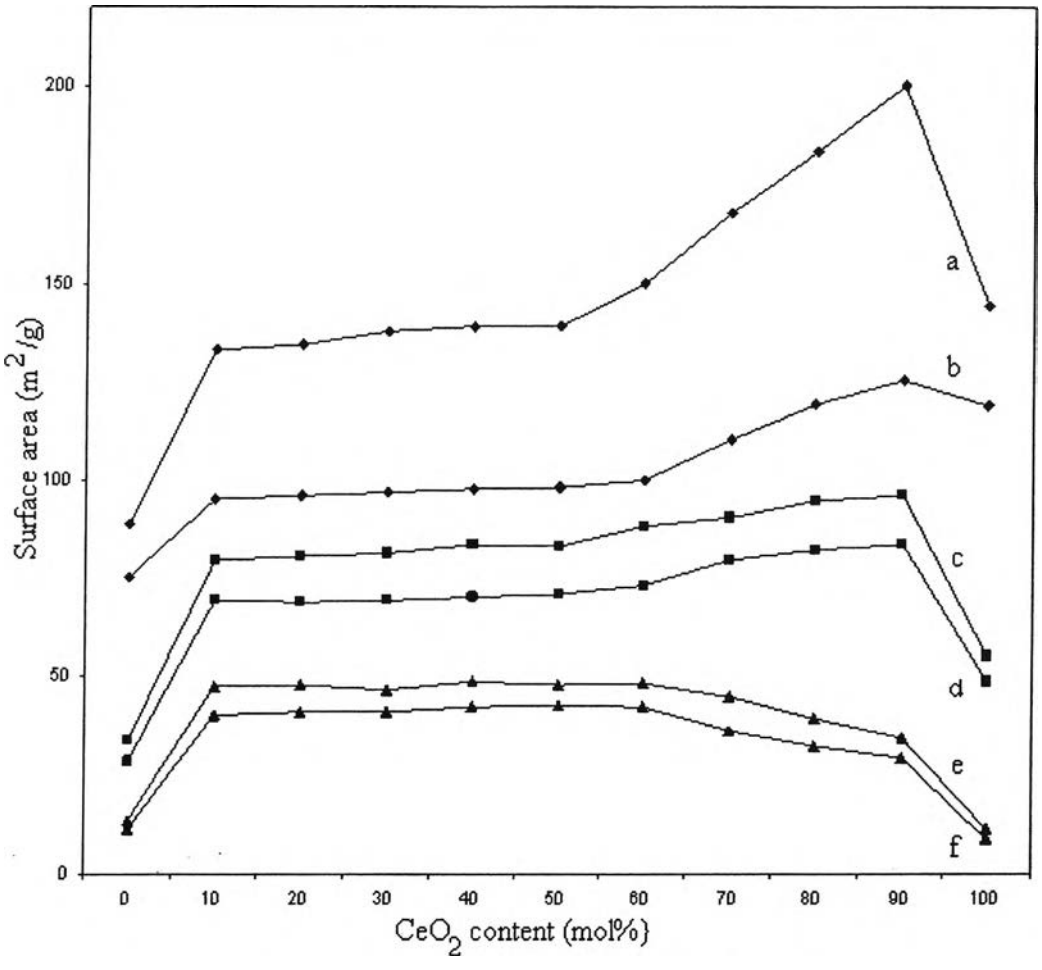

Figure 3.6 Surface area evolution as a function of composition for the samples aged for 24 h and calcined at (a) 500°C, (c) 700°C and (e) 900°C, and for the samples aged for 168 h and calcined at (b) 500°C, (d) 700°C and (f) 900°C.

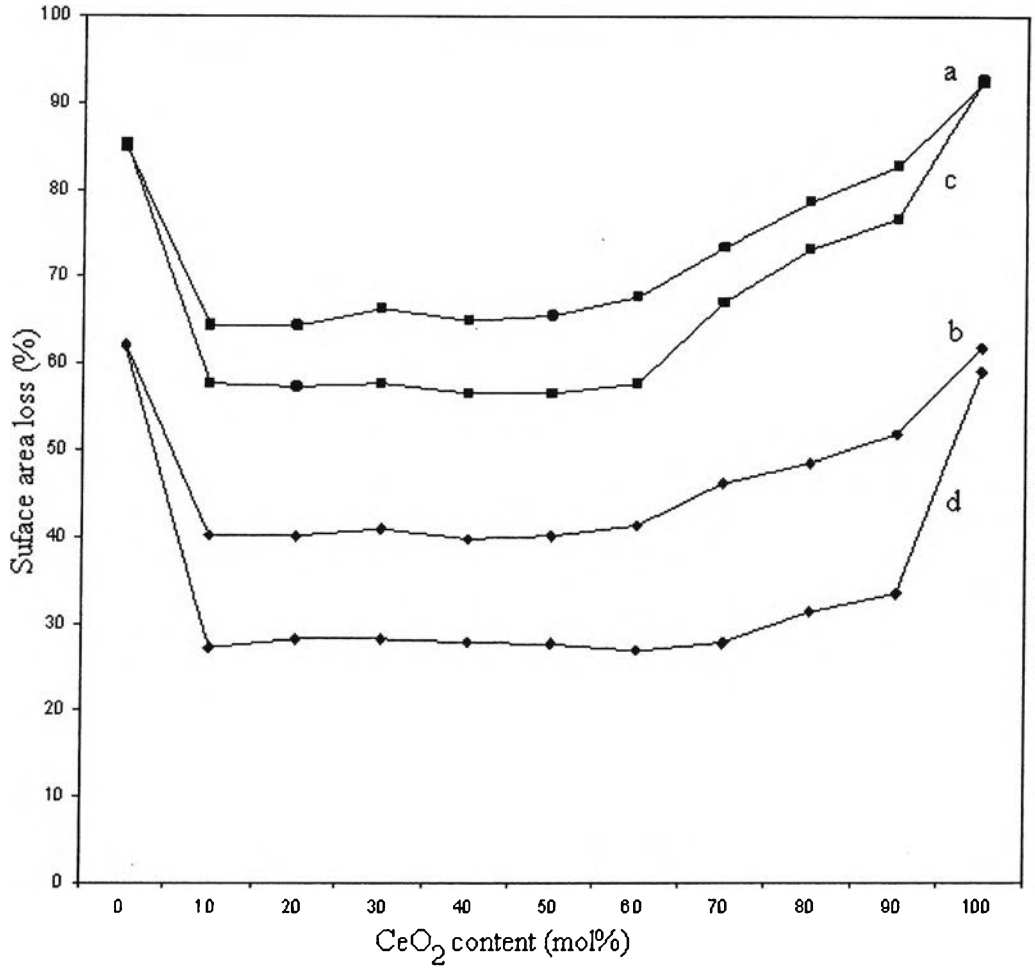

Figure 3.7 Loss of surface areas due to calcinations (from 500°C to 700°C and 900°C) for the samples aged for 24 h and calcined at (a) 900°C, (b) 700°C and the samples aged for 168 h and calcined at (c) 900°C, (d) 700°C.

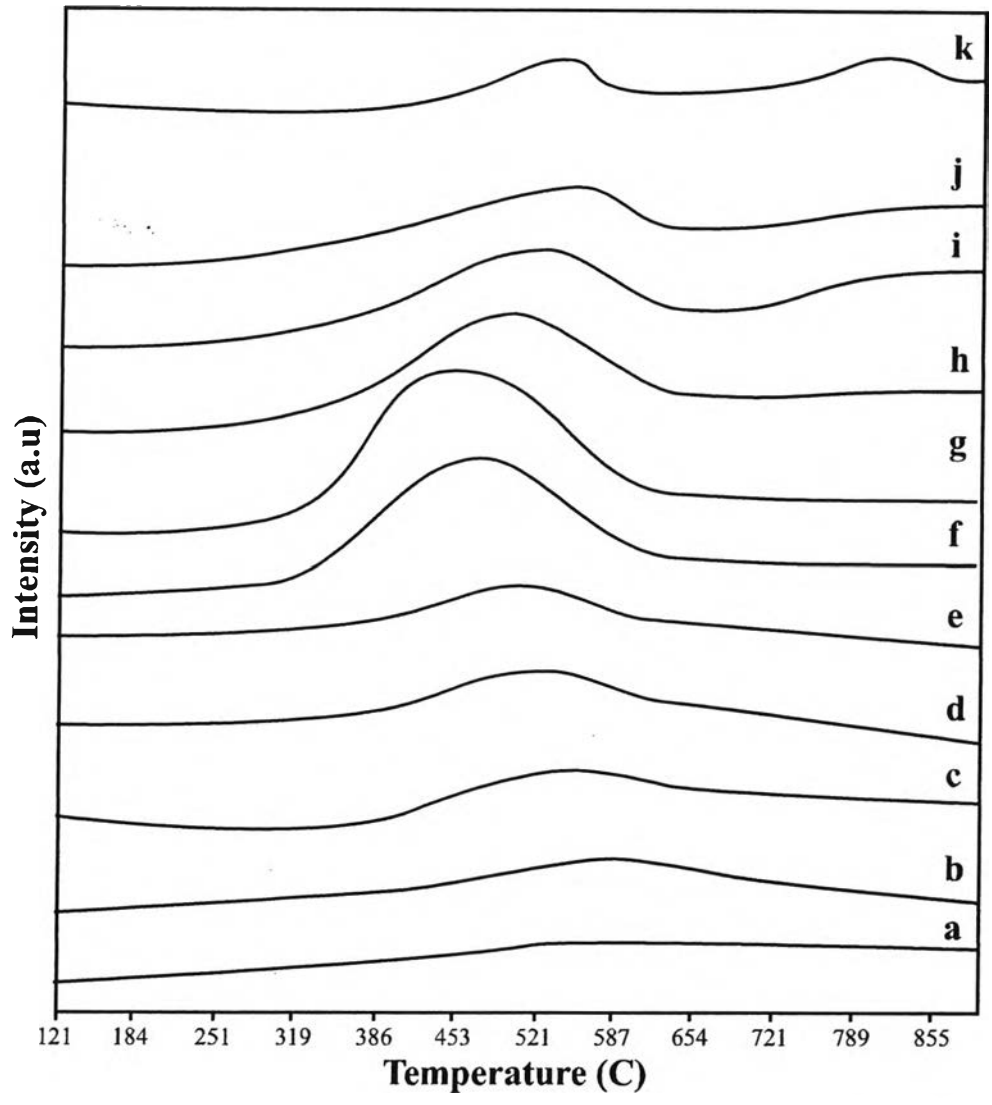

Figure 3.8 TPR profiles of ceria-zirconia mixed oxides with the aging time = 24 h and calcined at 900°C: (a) ZrO_2; (b) $Ce_{0.1}Zr_{0.9}$; (c) $Ce_{0.2}Zr_{0.8}$; (d) $Ce_{0.3}Zr_{0.7}$; (e) $Ce_{0.4}Zr_{0.6}$; (f) $Ce_{0.5}Zr_{0.5}$; (g) $Ce_{0.6}Zr_{0.4}$; (h) $Ce_{0.7}Zr_{0.3}$; (i) $Ce_{0.8}Zr_{0.2}$; (j) $Ce_{0.9}Zr_{0.1}$; (k) CeO_2.

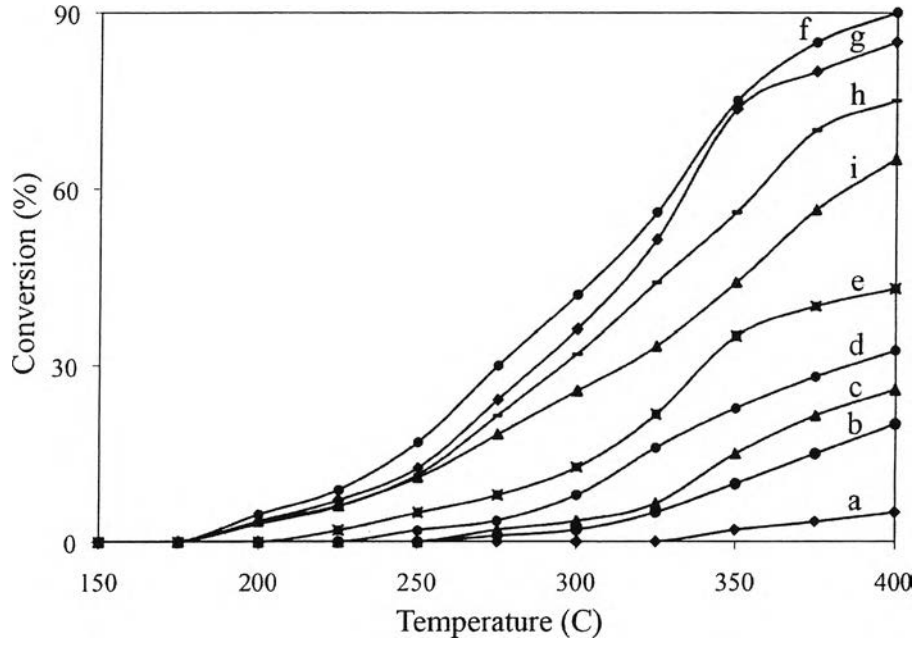

Figure 3.9 Light-off curves of ceria-zirconia mixed oxides with the aging time of 24 h and calcined at 500°C: (a) $Ce_{0.1}Zr_{0.9}$; (b) $Ce_{0.2}Zr_{0.8}$; (c) $Ce_{0.3}Zr_{0.7}$; (d) $Ce_{0.4}Zr_{0.6}$; (e) $Ce_{0.5}Zr_{0.5}$; (f) $Ce_{0.6}Zr_{0.4}$; (g) $Ce_{0.7}Zr_{0.3}$; (h) $Ce_{0.8}Zr_{0.2}$; (i) $Ce_{0.9}Zr_{0.1}$.

	X =								
	0.1	0.2	0.3	0.4	0.5	0.6	0.7	0.8	0.9
Ce (mol%)	9.84	21.23	30.67	40.67	51.02	61.51	72.16	81.22	92.15

Table 3.1 Practical compositions of $Ce_xZr_{1-x}O_2$ determined by XRF

Table 3.2 Average grain size (*D*) of $Ce_xZr_{1-x}O_2$

D (Å)	X =										
	0	0.1	0.2	0.3	0.4	0.5	0.6	0.7	0.8	0.9	1
Calcined at 700°C	8.11	7.20	5.04	4.21	3.55	3.98	4.12	5.35	6.76	9.05	11.89
Calcined at 900°C	18.87	18.00	17.02	12.55	12.43	13.15	14.08	15.65	17.04	17.45	21.05